

Strain-Induced Room-Temperature Ferroelectricity in SrTiO₃ Membranes

Ruijuan Xu^{*1,2}, Jiawei Huang³, Edward S. Barnard⁴, Seung Sae Hong^{1,2}, Prastuti Singh^{1,2},
Ed K. Wong⁴, Thies Jansen¹, Varun Harbola^{2,5}, Jun Xiao^{2,6}, Bai Yang Wang^{2,5}, Sam Crossley^{1,2},
Di Lu⁵, Shi Liu³, Harold Y. Hwang^{*1,2}

Email: rxu3@stanford.edu, hyhwang@stanford.edu

¹*Department of Applied Physics, Stanford University, Stanford, CA 94305, United States*

²*Stanford Institute for Materials and Energy Sciences, SLAC National Accelerator Laboratory,
Menlo Park, CA 94025, United States*

³*School of Science, Westlake University, Hangzhou, Zhejiang 310012, China*

⁴*The Molecular Foundry, Lawrence Berkeley National Laboratory, 1 Cyclotron Road, Berkeley,
CA 94720, United States*

⁵*Department of Physics, Stanford University, Stanford, CA 94305, United States*

⁶*Department of Materials Science and Engineering, Stanford University, Stanford, CA 94305,
United States*

Abstract

Advances in complex oxide heteroepitaxy have highlighted the enormous potential of utilizing strain engineering via lattice mismatch to control ferroelectricity in thin-film heterostructures. This approach, however, lacks the ability to produce large and continuously variable strain states, thus limiting the potential for designing and tuning the desired properties of ferroelectric films. Here, we observe and explore dynamic strain-induced ferroelectricity in SrTiO₃ by laminating freestanding oxide films onto a stretchable polymer substrate. Using a combination of scanning probe microscopy, optical second harmonic generation measurements, and atomistic modeling, we demonstrate robust room-temperature ferroelectricity in SrTiO₃ with 2.0% uniaxial tensile strain, corroborated by the notable features of 180° ferroelectric domains and an extrapolated transition temperature of 400 K. Our work reveals the enormous potential of employing oxide membranes to create and enhance ferroelectricity in environmentally benign lead-free oxides, which hold great promise for applications ranging from non-volatile memories and microwave electronics.

Transition metal oxides exhibit a diverse set of electrical, magnetic, and thermal properties and hold great promise for modern technological applications. Among these oxide materials, the perovskite SrTiO₃ has stimulated considerable interest as it hosts a rich spectrum of physical properties such as dilute superconductivity¹, multiple structural instabilities², and a variety of emergent phenomena arising from the interface of SrTiO₃-based heterostructures^{3,4,5,6,7}. In addition, SrTiO₃ is also one of the few known quantum paraelectric materials, in which quantum fluctuations and antiferrodistortive instabilities suppress ferroelectric polar order at low temperature, thus resulting in a non-polar paraelectric state^{8,9}. Despite the intrinsic paraelectric nature of SrTiO₃, it is possible to stabilize ferroelectric order via a variety of means such as substrate-induced strain^{10,11,12,13,14}, cation doping¹⁵, ¹⁸O isotope substitution¹⁶, and defect engineering¹⁷, etc. In particular, advances in thin-film epitaxy have highlighted the role of substrate-induced strain in stabilizing ferroelectricity and enhancing the ferroelectric transition temperature T_c in SrTiO₃ thin-film heterostructures. This strategy of ‘strain engineering’ relies on the lattice mismatch between the film and the underlying substrate, and has been widely used in tuning the structure and properties of many oxide materials^{18,19,20,21}. However, due to the limited number of commercially available substrates and defect-induced strain relaxation during growth²², this approach is fundamentally limited in its lack of ability to produce large and continuously tunable strain states. These constraints in turn limit the strain range that could be realized in practice, restricting the rational design and control of desired material properties via strain.

The advent of freestanding crystalline oxide membrane films presents enticing new possibilities to address these challenges and develop new degrees of freedom to manipulate material properties. In particular, the recently developed water-soluble pseudoperovskite Sr₃Al₂O₆ has become widely used as a sacrificial buffer layer in the fabrication of a variety of freestanding,

crystalline oxide thin films^{23,24,25,26,27,28}. These freestanding films, with millimeter-scale lateral dimensions and down to nanometer-scale thickness, can accommodate much larger strains than their bulk counterparts^{29,30,31}. Here, we integrate the freestanding SrTiO₃ films onto a flexible polymer stretching platform to probe the strain-tunable ferroelectric transition in SrTiO₃³⁰. In this work, using a variety of characterization techniques we demonstrate robust room-temperature ferroelectricity in SrTiO₃ with 2.0% uniaxial tensile strain, which is corroborated by the notable features of 180° ferroelectric domains and an extrapolated transition temperature of 400 K.

First, we prepared an epitaxial heterostructure of 14 nm SrTiO₃ thin films with a 16 nm Sr₂CaAl₂O₆ sacrificial buffer layer synthesized on single-crystalline SrTiO₃ substrates via reflection high-energy electron diffraction (RHEED) - assisted pulsed laser deposition (Supplementary Fig. 1). We substituted Ca into Sr₃Al₂O₆ to modify the lattice parameter of the sacrificial layer to closely match the SrTiO₃ lattice (the lattice constant of Sr₂CaAl₂O₆ is 15.6 Å, which is close to 4 times the lattice constant of SrTiO₃). Doing so can effectively reduce the lattice mismatch between different layers and minimize the crack formation in released freestanding films²⁷. After fully dissolving Sr₂CaAl₂O₆ in deionized water, the SrTiO₃ film is released from the substrate and transferred onto a flexible polyimide sheet that can be stretched into various strain states (see methods and Fig. 1a). The interface between the SrTiO₃ membrane and the polyimide sheet provides strong interface adhesion, enabling the success of the strain experiment. Using both an optical microscope and atomic force microscopy, we characterized the topography of the resulting freestanding membranes and noted that the millimeter scale films (laterally) are free of cracks in their unstrained state (Fig. 1b-d). Since strain relaxation occurs in the vicinity of cracks³², these crack-free SrTiO₃ membranes are able to preserve homogeneous strain, presenting an ideal platform for our strain experiments. Additionally, a two-dimensional array of gold electrodes was

evaporated on the membrane surface using electron-beam evaporation with a shadow mask. These electrodes serve as optical markers to measure strain in the strain experiment (Fig. 1c).

Next, we conducted piezoresponse force microscopy (PFM) to explore how strain affects ferroelectric order in SrTiO₃ membranes. Here, the flexible polyimide sheet allows the strain state to be flexibly manipulated. In this work, we focus on the case of in-plane uniaxial tensile strain by stretching the membrane along the [100] direction, while supplying a small amount of tensile stress to keep the membrane undeformed along the other orthogonal in-plane direction. Note that it is usually difficult to create such a highly anisotropic strain geometry using commercially available substrates. The strain state was characterized optically by measuring the change in spacing between gold markers (i.e. $\varepsilon = \Delta l/l$, Fig. 2a), and further microscopically confirmed by grazing incidence X-ray diffraction (GIXRD) measurements³⁰ (see methods and Fig. 2b-d). Here, with increasing strain, the GIXRD peak measured along the [100] strain direction shifts towards lower angles, indicating the increase in the lattice parameter upon stretching, whereas the peak position measured along the [010] direction remains almost unchanged. It is also noted that the uniaxial strain values measured by GIXRD closely match with the optically measured strain values. In order to maintain the strain state of the film even after removing the external stress from membranes, the adhesive polycaprolactone was used in its melted liquid form to bond the stretched membrane onto a rigid substrate at 110 °C, and then cooled to room-temperature to lock-in the strain state (see methods). Using this strain setup, we characterize the ferroelectric properties of strained SrTiO₃ via PFM at room temperature (see methods). In a small strain state ($\varepsilon \leq 1.25\%$), we measured very weak signals from the membrane, indicating the absence of ferroelectricity at room temperature within this strain range (Fig. 2e-g and Supplementary Fig. 2). By contrast, for larger strain ($\varepsilon > 1.5\%$), we observed strong lateral signals from membranes with notable stripe

domain patterns, which indicates the emergence of room-temperature ferroelectricity (Fig. 2h, i and Supplementary Fig. 2). The observed polydomain structures, which are only observable from lateral piezoresponse, are in-plane polarized due to the tensile strain.

Since lateral PFM imaging is carried out via the torsional movement of the PFM cantilever in response to shear deformation of in-plane polarized domains, in-plane piezoresponse signals will vanish when the cantilever is aligned along the in-plane polarization direction. Therefore, by varying the relative orientation between the cantilever and the sample, we can determine the actual polarization direction (Supplementary Fig. 3). Using this approach, we found that the ferroelectric polarization of SrTiO₃ membranes is along [100]/[$\bar{1}00$] with the adjacent domains polarized at a 180° difference, which coincides with the uniaxial tensile strain direction (Fig. 2j). These PFM results provide direct evidence of robust room-temperature ferroelectricity in strained SrTiO₃ membranes, corroborated by the notable 180° ferroelectric polydomain structures. The observed in-plane polarized 180° domain structure with only one in-plane polarization variant (along the [100]/[$\bar{1}00$] directions) is rather rare not just in SrTiO₃ but also in other ferroelectric perovskites such as PbTiO₃, BaTiO₃, etc. The ability in this work to artificially create such domain structure provides the opportunity for exploring and controlling new functionalities in ferroelectrics, which could become potential candidates for device elements in next-generation nanoelectronics such as in-plane ferroelectric non-volatile memories. Moreover, we find that the SrTiO₃ membranes can sustain beyond 2.0% uniaxial tensile strain without fracture, which exceeds the reported maximum substrate-induced tensile strain in SrTiO₃ heterostructures¹⁰ (i.e., 1.0% for SrTiO₃ films grown on DyScO₃ (110)). Abrupt crack formation occurs typically above 2.5% strain in SrTiO₃ membranes, giving rise to paraelectricity in SrTiO₃ at room temperature due to strain relaxation (Supplementary Fig. 4).

We further performed temperature-dependent optical second harmonic generation (SHG) measurements to explore the strain-induced variation of T_c in the SrTiO₃ membranes. In our SHG measurements, a 900 nm fundamental beam is used to excite the SHG signal from the membrane in a reflection geometry that can be probed at a wavelength of 450 nm (see methods and Fig. 3a). First, in order to understand the structural symmetry of the strain-induced ferroelectric phase, we carried out SHG measurements in strained membranes that exhibit room-temperature ferroelectricity ($\varepsilon \geq 1.5\%$) as a function of incident beam polarization (Supplementary Fig. 5). The intensity of the output SHG signals is detected at a polarizer angle which is either parallel (I_x , Fig. 3b) or perpendicular (I_y , Fig. 3b) to the uniaxial strain direction in membranes. By analyzing these polar plots using the symmetry-based SHG tensor, we find that the ferroelectric phase is in the orthorhombic $mm2$ point group symmetry with the polar axis aligned in-plane along the uniaxial strain direction³³ (see methods), which is consistent with our PFM observations. Next, we measured the ferroelectric T_c of strained membranes by probing SHG as a function of temperature. Since the adhesive used in our strain setup softens and allows strain relaxation above 60°C, our measurements were limited to temperatures below this scale. We probed the T_c of membranes strained to $\varepsilon = 0.5\%$, 0.9% , and 1.25% , wherein the SHG intensity decreases with temperature and gradually vanishes at a critical temperature which indicates the onset of the phase transition (Fig. 3c and Supplementary Fig. 6). Plotting the integrated SHG peak intensity as a function of temperature for each strain state, we can extract T_c using a temperature-dependent order parameter fit derived from the Ginsburg-Landau-Devonshire (GLD) model (see methods and Supplementary Fig. 7). Our results reveal that the measured T_c increases linearly with strain, which agrees well with the theoretical value predicted by the GLD model (see methods, Fig. 3d and Supplementary Fig. 8). Following this theoretical trend, we can also estimate T_c for membranes with a phase

transition far above room temperature ($\epsilon \geq 1.5\%$, Fig. 3d). Our results indicate that for 2.0%, T_c extrapolates to 400 K, i.e. robust room-temperature ferroelectricity. Additionally, these results also indicate that it is possible to directly tune the transition temperature in a deterministic manner.

To understand the origin of the strain-driven ferroelectric phase and the nature of the phase transition in strained SrTiO₃ membranes, we performed first-principles density functional theory (DFT) calculations and molecular dynamics (MD) simulations. We calculated the energy of the paraelectric and ferroelectric phase in SrTiO₃ as a function of strain using DFT calculations with a 5-atom unit cell and local density approximation (LDA) (see methods and Fig. 4a). DFT calculations reveal that the ferroelectric phase is favored over the paraelectric phase by a small energy difference when the applied strain is greater than 0.25%. Also, consistent with our experimental observations, DFT calculations indicate that uniaxial tensile strain along the [100] direction induces polarization along this direction, and the induced polarization is a result of the displacement of both the Sr and Ti atoms away from the center of the surrounding oxygen lattice (Supplementary Fig. 9, Table 1, and Supplementary Data). Next, slab-model MD simulations were performed to understand the nature of temperature-driven phase transitions in 2.0% uniaxially strained SrTiO₃ membranes. In order to obtain atomistic insights into the nature of the phase transition, we calculated the probability distribution of the unit cells adopting a [100]-component of local polarization as a function of temperature (Fig. 4b). At low temperature, the distribution of local polarization in the ferroelectric phase is Gaussian-like with a single peak at $\approx 0.3 \text{ C/m}^2$ (120 K, Fig. 4b). With increasing temperature, the peak shifts towards a lower polarization value, indicating the displacive character of the phase transition (e.g., 140 K and 160 K, Fig. 4b). At 180 K, another peak located near -0.18 C/m^2 emerges, suggesting the onset of an order-disorder phase transition (180 K, Fig. 4b). In the high temperature paraelectric phase (240 K and 300 K, Fig. 4b),

the distribution becomes a double-peaked curve (again an indicator of the order-disorder transition) but with a non-zero probability at $P = 0$ (an indicator of the displacive transition),³⁴ indicating a notable mixture of displacive and order-disorder characteristics of the phase transition in SrTiO₃ (Supplementary Fig. 10). Snapshots of the dipole configuration from MD simulations further illustrate such mixed transition character (Fig. 4c). For instance, the snapshot obtained at 120 K shows a typical ferroelectric phase with the majority of unit cells polarized along [100]. As the temperature increases, the orientation of the dipoles become more disordered but the long-range correlation still remains along [100]. At 300 K the macroscopic paraelectricity arises as an ensemble-averaged result of randomly oriented local dipoles¹⁷, including both the nearly zero and non-zero dipoles, resulting in a zero-net polarization.

To conclude, we observe direct evidence of robust room-temperature ferroelectricity in strained SrTiO₃ membranes, corroborated by 180° domain formation and the evolution of T_c with strain. Using SrTiO₃ membranes as a promising example, our work demonstrates the significant potential of employing oxide membranes for enhanced ferroelectric properties in diverse oxide materials. These significant enhancements in ferroelectric polarization and T_c hold great promise for non-volatile ferroelectric memory applications. The ability to obtain extreme and continuously tunable strain states with freestanding membranes also provides broad opportunities for achieving high dielectric tunability at room temperature, which is important for microwave electronics such as tunable capacitors and phase shifters, etc³⁵. In addition, combining the nanoscale freestanding film with the flexible polymer substrate allows the strain state to be manipulated to arbitrary geometries and anisotropies, which provides new degrees of freedom for creating topologically nontrivial polar structures and functional domain walls coupled with potentially large dielectric, piezoelectric, and magnetic responses^{36,37}. Moreover, the polymer substrates which are stretched

in the elastic deformation regime allows the reversible control of the phase transition and their associated dielectric and piezoelectric responses, providing new possibilities for designing a variety of strain-tunable ferroelectric devices.

Methods

Thin Film Growth. The epitaxial heterostructure of 14 nm SrTiO₃ films was synthesized with a 16 nm Sr₂CaAl₂O₆ sacrificial layer on (001)-oriented single-crystalline SrTiO₃ substrates via RHEED - assisted pulsed-laser deposition. The growth of the Sr₂CaAl₂O₆ layer was carried out in dynamic argon pressure of 4×10^{-6} torr, at a growth temperature of 710 °C, a laser fluence of 1.35 J/cm², and a repetition rate of 1 Hz, using a 4.8 mm² imaged laser spot. The growth of the SrTiO₃ layer was conducted in dynamic oxygen pressure of 4×10^{-6} torr, at a growth temperature of 710 °C, a laser fluence of 0.9 J/cm², and a repetition rate of 1 Hz, using a 3.0 mm² imaged laser spot.

SrTiO₃ Membrane Fabrication. The heterostructure was first attached to a polymer support of 100 μm thick polypropylene carbonate (PPC) film and placed in deionized water at room temperature until the sacrificial Sr₂CaAl₂O₆ layer was fully dissolved. The PPC coated SrTiO₃ film was then released from the substrate and transferred onto a polyimide sheet. Finally, the PPC layer was removed from the membrane through thermal decomposition in O₂ at 260 °C for 2 hours.

Stretching Experiment. We applied uniaxial stress to SrTiO₃ membranes along [100] directions via micromanipulators to stretch the polyimide substrate, while keeping the membrane undeformed along the other orthogonal in-plane direction by applying a small amount of compensating stress along [010]. The resultant strain was characterized using optical microscopy to measure the change in spacing between circular gold markers, which were evaporated with a shadow mask using e-beam evaporation. In order to preserve the strain state in SrTiO₃, polycaprolactone was used in its melted liquid form to bond the strained oxide/polymer bilayer to a ceramic chip carrier at 110 °C. Polycaprolactone solidifies by cooling the strain setup to room

temperature, which freezes the strain state of the SrTiO₃ membranes, and is stable on the ~ 2 week time scale.

Crystal Structure Characterization. Grazing incidence x-ray diffraction measurements were performed using high-resolution X-ray diffractometer (PANalytical X'Pert Pro MRD). The measurement geometry was configured in the in-plane diffraction mode to allow X-rays to probe the crystal lattice along the in-plane directions.

Domain Structure Characterization. The PFM studies were carried out with a Cypher AFM (Asylum Research) using Ir/Pt-coated conductive tips (Nanosensor, PPP-EFM, force constant ≈ 2.8 N/m). The vector PFM mode was used to image both the out-of-plane and in-plane domain structure simultaneously.

Optical Second Harmonic Generation Measurements. In SHG measurements we illuminated the sample with a Coherent Chameleon Ultra II Ti: Sapphire laser tuned to 900 nm wavelength and focused onto the sample with a $20 \times$ NA= 0.45 ELWD Nikon objective. The temperature dependent SHG measurements were performed using a modified Janus ST500 Optical Vacuum Cryostat. Input polarization was controlled by the rotation of a half waveplate in the laser beam path. The generated SHG signals were collected on an Andor iXon CCD and Kymera Spectrometer.

The analysis of SHG intensity polar plots was performed using the symmetry-based SHG tensor. For the in-plane polarized domains, the fundamental beam produces electric field components which can be described as $E^\omega(\varphi) = (-E_0 \sin\varphi, 0, E_0 \cos\varphi)$, where φ is the azimuthal angle of the fundamental light polarization shown in Fig. 3b. The light-induced non-linear polarization of the in-plane polarized domains can be described using the $mm2$ point group-based SHG tensor:

$$\begin{pmatrix} P_1 \\ P_2 \\ P_3 \end{pmatrix} = \begin{pmatrix} 0 & 0 & 0 & 0 & d_{15} & 0 \\ 0 & 0 & 0 & d_{24} & 0 & 0 \\ d_{31} & d_{32} & d_{33} & 0 & 0 & 0 \end{pmatrix} \begin{pmatrix} E_1^2 \\ E_2^2 \\ E_3^2 \\ 2E_2E_3 \\ 2E_1E_3 \\ 2E_1E_2 \end{pmatrix} \quad (1)$$

where $E_1 = -E_0 \sin \varphi$, $E_2 = 0$, and $E_3 = E_0 \cos \varphi$. Since the output polarizer is placed either parallel (I_x , Fig. 3b) or perpendicular (I_y , Fig. 3b) to the in-plane uniaxial strain direction (polarization direction) in the membrane, the output SHG signal can be described as $I_x^{2\omega}(\varphi) = I_3^{2\omega} \propto (\mathbf{P}^{2\omega} \cdot \mathbf{A}_x)^2 = (d_{33}E_0^2 \cos^2 \varphi + d_{31}E_0^2 \sin^2 \varphi)^2$ and $I_y^{2\omega}(\varphi) = I_1^{2\omega} \propto (\mathbf{P}^{2\omega} \cdot \mathbf{A}_y)^2 = (d_{15}E_0^2 \sin 2\varphi)^2$, where $\mathbf{A}_x = (0,0,1)$ and $\mathbf{A}_y = (1,0,0)$. The experimental polar plots can be well fitted using the derived $I_x^{2\omega}(\varphi)$ and $I_y^{2\omega}(\varphi)$, indicating the strained SrTiO₃ is in the orthorhombic $mm2$ point group symmetry. Detailed fitting analysis can be found in reference [33]. Note that the tetragonal $4mm$ point group-based SHG tensor also generates similar fitting results. But given the experimental strain geometry where the membrane elongates along the in-plane uniaxial strain direction while compresses along the out-of-plane direction due to the Poisson effect (we keep the membrane undeformed along the other orthogonal in-plane direction), the possibility of the tetragonal $4mm$ point group symmetry is thus ruled out from our analysis.

Ginsburg-Landau-Devonshire Calculations. In this model, we used the power-series expansion of the Helmholtz free energy F in terms of polarization components P_i and structural order parameters Q_i ($i = 1, 2, 3$), which is expressed as follows³⁸:

$$\begin{aligned} F = & \alpha_1(P_1^2 + P_2^2 + P_3^2) + \alpha_{11}(P_1^4 + P_2^4 + P_3^4) + \alpha_{12}(P_1^2P_2^2 + P_1^2P_3^2 + P_2^2P_3^2) + \beta_1(Q_1^2 + \\ & Q_2^2 + Q_3^2) + \beta_{11}(Q_1^4 + Q_2^4 + Q_3^4) + \beta_{12}(Q_1^2Q_2^2 + Q_1^2Q_3^2 + Q_2^2Q_3^2) + 1/2 c_{11}(S_1^2 + S_2^2 + S_3^2) + \\ & c_{12}(S_1S_2 + S_1S_3 + S_2S_3) + 1/2 c_{44}(S_4^2 + S_5^2 + S_6^2) - g_{11}(S_1P_1^2 + S_2P_2^2 + S_3P_3^2) - g_{12}[S_1(P_2^2 + \\ & P_3^2) + S_2(P_1^2 + P_3^2) + S_3(P_1^2 + P_2^2)] - g_{44}(S_4P_2P_3 + S_5P_1P_3 + S_6P_1P_2) - \lambda_{11}(S_1Q_1^2 + S_2Q_2^2 + \end{aligned}$$

$$\begin{aligned}
& S_3 Q_3^2) - \lambda_{12}[S_1(Q_2^2 + Q_3^2) + S_2(Q_1^2 + Q_3^2) + S_3(Q_1^2 + Q_2^2)] - \lambda_{44}(S_4 Q_2 Q_3 + S_5 Q_1 Q_3 + \\
& S_6 Q_1 Q_2) - t_{11}(P_1^2 Q_1^2 + P_2^2 Q_2^2 + P_3^2 Q_3^2) - t_{12}[P_1^2(Q_2^2 + Q_3^2) + P_2^2(Q_1^2 + Q_3^2) + P_3^2(Q_1^2 + Q_2^2)] - \\
& t_{44}(P_1 P_2 Q_1 Q_2 + P_1 P_3 Q_1 Q_3 + P_2 P_3 Q_2 Q_3), \tag{2}
\end{aligned}$$

where S_n ($n = 1, 2, 3, 4, 5, 6$) are lattice strains, c_{nl} are the elastic stiffnesses, g_{nl} are the electrostrictive constants, λ_{nl} are the linear-quadratic coupling coefficients between the strain and structural order parameters, and t_{nl} are the coupling coefficients between the polarization and structural order parameters.

In order to simplify the analysis, we considered the scenario where there is no antiferrodistortive structural transition, i.e., $Q_i = 0$ ($i = 1, 2, 3$). In that case equation (2) can be written in the following format:

$$\begin{aligned}
F = & \alpha_1(P_1^2 + P_2^2 + P_3^2) + \alpha_{11}(P_1^4 + P_2^4 + P_3^4) + \alpha_{12}(P_1^2 P_2^2 + P_1^2 P_3^2 + P_2^2 P_3^2) + \\
& 1/2 c_{11}(S_1^2 + S_2^2 + S_3^2) + c_{12}(S_1 S_2 + S_1 S_3 + S_2 S_3) + 1/2 c_{44}(S_4^2 + S_5^2 + S_6^2) - g_{11}(S_1 P_1^2 + \\
& S_2 P_2^2 + S_3 P_3^2) - g_{12}[S_1(P_2^2 + P_3^2) + S_2(P_1^2 + P_3^2) + S_3(P_1^2 + P_2^2)] - g_{44}(S_4 P_2 P_3 + S_5 P_1 P_3 + \\
& S_6 P_1 P_2). \tag{3}
\end{aligned}$$

Given the experimentally used in-plane uniaxial strain geometry, we considered the case of $S_1 \neq 0$, $S_2 = 0$, and $S_3 \neq 0$. In addition, in this case the shear strain S_6 is zero³⁸. For the experimentally observed 180° ferroelectric domains, we can simplify the problem with the consideration of only one polarization component along the uniaxial strain direction, i.e., $P_1 \neq 0$, $P_2 = P_3 = 0$. Therefore, the equation (3) can be further simplified as:

$$\begin{aligned}
F = & \alpha_1 P_1^2 + \alpha_{11} P_1^4 + 1/2 c_{11}(S_1^2 + S_3^2) + c_{12} S_1 S_3 + 1/2 c_{44}(S_4^2 + S_5^2) - \\
& (g_{11} S_1 + g_{12} S_3) P_1^2. \tag{4}
\end{aligned}$$

Next, using the relation $\frac{\partial F}{\partial S_3} = \frac{\partial F}{\partial S_4} = \frac{\partial F}{\partial S_5} = 0$, which is derived from the mechanical boundary condition $\sigma_3 = \sigma_4 = \sigma_5 = 0$, we can derive the following relations:

$$c_{11}S_3 + c_{12}S_1 - g_{12}P_1^2 = 0; \quad (5)$$

$$c_{44}S_4 = 0; \quad (6)$$

$$c_{11}S_5 = 0. \quad (7)$$

From these relations, we can further derive $S_4 = S_5 = 0$ and $S_3 = \frac{g_{12}P_1^2 - c_{12}S_1}{c_{11}}$. Using these values in equation (4), we can re-write the free energy in the following form with renormalized expansion coefficients:

$$F = \alpha'_{11}P_1^4 + \alpha'_1P_1^2 + C, \quad (8)$$

where $\alpha'_{11} = \alpha_{11} - \frac{g_{12}^2}{2c_{11}}$, $\alpha'_1 = \alpha_1 - g_{11}S_1 + \frac{g_{12}c_{12}S_1}{c_{11}}$, $C = \frac{1}{2}c_{11}S_1^2 - \frac{c_{12}^2S_1^2}{2c_{11}}$.

For the in-plane uniaxial strain geometry used in our experiment, $S_l = S_u$ where S_u is the uniaxial strain state. Using the thermodynamic parameters³⁸ (Supplementary Table 2) in equation (8), F becomes a function of P_l , S_u , and temperature T (since α_1 relates to temperature). By calculating the minima of F with respect to P_l , we can find the relation between P_l and T at a given S_u :

$$P_1^2 = \frac{\left(g_{11} - \frac{g_{12}c_{12}}{c_{11}}\right)S_u - \alpha_1}{2\alpha_{11} - \frac{g_{12}^2}{c_{11}}}, \quad (9)$$

where $\alpha_1 = 4.5[\coth\left(\frac{54}{T}\right) - \coth\left(\frac{54}{30}\right)] \times 10^{-3}$.

Such a relation is plotted in Supplementary Fig. 8, which allows us to extract T_c at $P_l = 0$ as a function of S_u (Fig. 3d).

First-Principles Density Functional Theory Calculations. First-principles DFT calculations were performed with QUANTUM-ESPRESSO³⁹ package using the local density approximation (LDA)⁴⁰ and ultrasoft pseudopotentials from the Garrity, Bennet, Rabe, Vanderbilt

(GBRV) high-throughput pseudopotential set⁴¹. We used an $8 \times 8 \times 8$ Monkhorst-Pack k -point mesh⁴² for Brillouin-zone sampling and a plane-wave cutoff of 50 Ry and a charge density cutoff of 250 Ry. A force convergence threshold of 1.0×10^{-4} Ry/Bohr, a pressure convergence threshold of 0.5 kbar, and Marzari-Vanderbilt smearing⁴³ of 1 mRy were used to optimize the atomic positions and lattice constants. In order to simplify the analysis, we use a 5-atom unit cell model, which rules out the possible effects of oxygen octahedral rotation, a known antiferroelectric mode in SrTiO₃. Our simplification is justified as the unstrained structure of interest in the experiment is cubic SrTiO₃ in which the oxygen octahedral rotation is zero above 105 K. The LDA lattice constant of cubic SrTiO₃ is 3.857 Å, which is consistent with previous theoretical results⁴⁴ and close to the experimental value of 3.905 Å. Following the experimental setup, the uniaxial strain state is induced by fixing the lattice constant b along [010] to its ground-state value while fixing the lattice constant a along [100] to a uniformly spaced grid sampled between 3.838 Å and 3.934 Å (corresponding to a strain range from -0.5% to 2.0% in reference to the DFT ground-state cubic structure) with a step size of 0.002 Å. For a given combination of (a, b) , the perpendicular lattice constant c and internal coordinates are fully relaxed to obtain the most stable structure under the given strain condition. The polarization is then estimated using the Born effective charges and the atomic positions. The detailed structural information can be found in the provided crystallographic information files (Supplementary Data).

Molecular Dynamics Simulations. MD simulations of SrTiO₃ were performed using a bond-valence-based atomistic potential parameterized from first-principles calculations^{34,45}. This force field was able to reproduce both composition- and temperature-driven phase transitions of the Ba_xSr_{1-x}TiO₃ solid solution⁴⁶ and has been successfully used to describe the THz-driven transient ferroelectric phase in SrTiO₃⁴⁷. In order to model SrTiO₃ thin films without periodicity

in the direction perpendicular to the surface, we constructed a supercell containing a SrTiO₃ slab of 90,000 atoms (30 × 20 × 30 cells) adjacent to a vacuum region. The SrTiO₃ slab, which is 20 unit-cells in thickness, has the surface normal along the [010] direction. The vacuum along the surface normal is 85.4 Å thick, which is sufficiently large to prevent spurious interactions between neighboring periodic images. To stabilize the thin film in vacuum, the bond-valence charges of the surface layers were reduced by a factor of two, following a similar protocol developed in reference [48]. In order to investigate the nature of temperature-driven phase transitions in strained SrTiO₃ membranes, we first equilibrated the slab model by running NVT (constant-volume constant-temperature) simulation using a time-step of 1 fs with a 2.0% tensile strain along the [100] direction. The temperature was controlled via the Nosé-Hoover thermostat⁴⁹ implemented in Large-scale Atomic/Molecular Massively Parallel Simulator (LAMMPS)⁵⁰. To facilitate the equilibrium process, a small bias field was applied along the [100] direction for 50 ps after which another equilibrium run of 50 ps was performed with the bias field turned off. The final equilibrium structure is a single domain with the polarization along the [100] direction. Then we increased temperature gradually to explore the temperature-driven ferroelectric phase transition in strained SrTiO₃ membranes.

Data availability

Crystallographic data in this study are provided in Supplementary Data. The data that support the findings of this study are available from the corresponding author upon reasonable request.

Figures

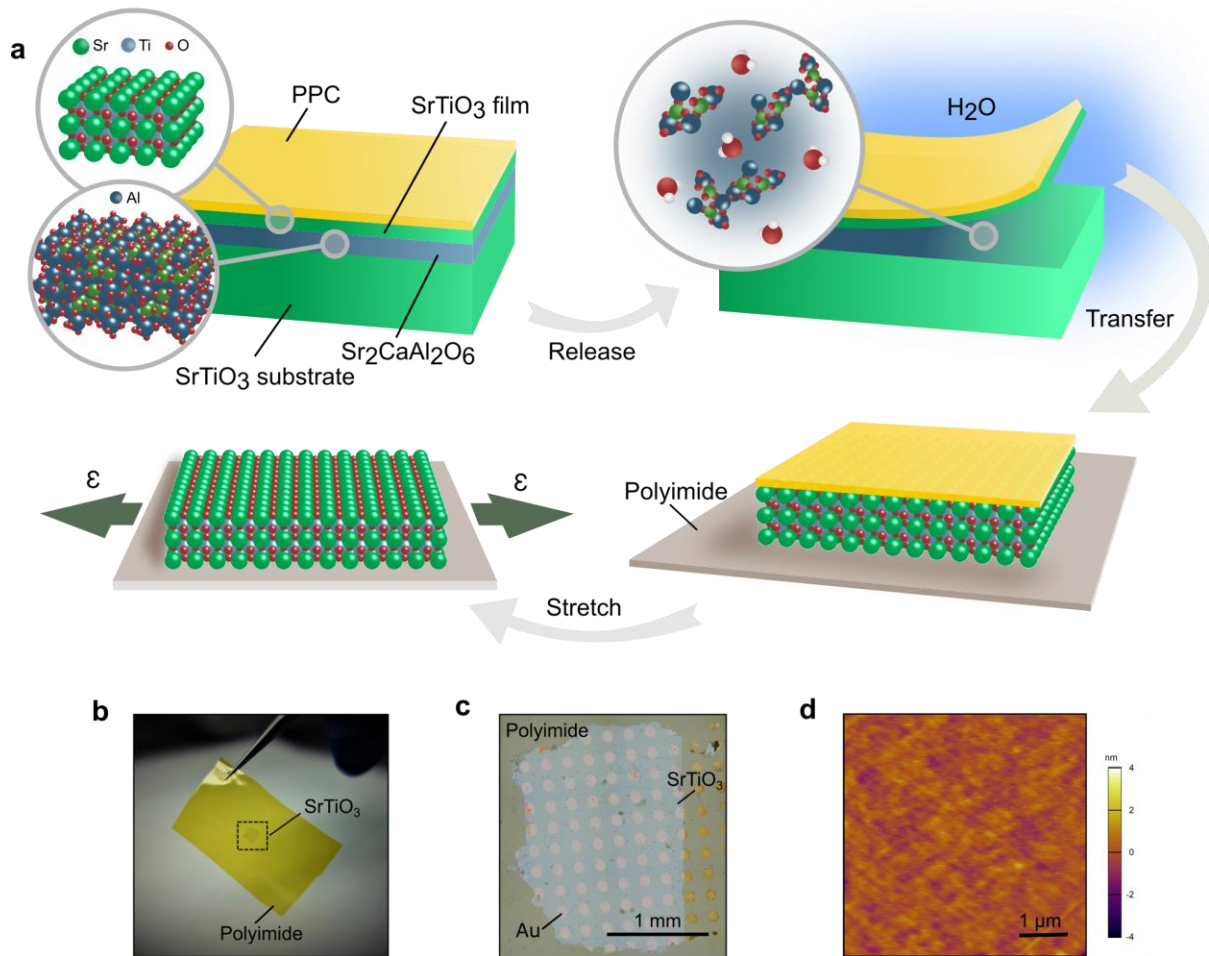


Figure 1 | Preparation of freestanding SrTiO₃ membranes. **a**, Schematic illustrating the lift-off and transfer process for SrTiO₃ membranes onto polyimide sheets. By dissolving the sacrificial layer Sr₂CaAl₂O₆ from the as-grown heterostructure, SrTiO₃ films can be released and transferred onto a polyimide sheet with a layer of polypropylene carbonate (PPC) as the supporting material. The oxide/polymer bilayer structure can be stretched after the PPC is thermally decomposed in O₂. Optical images of the transferred millimeter-scale freestanding SrTiO₃ membranes are shown in **b** and **c** with an ordered array of gold as optical markers. **d**, Detailed atomic force microscopy topographic images reveal the crack-free surface of SrTiO₃ transferred onto the polyimide sheet.

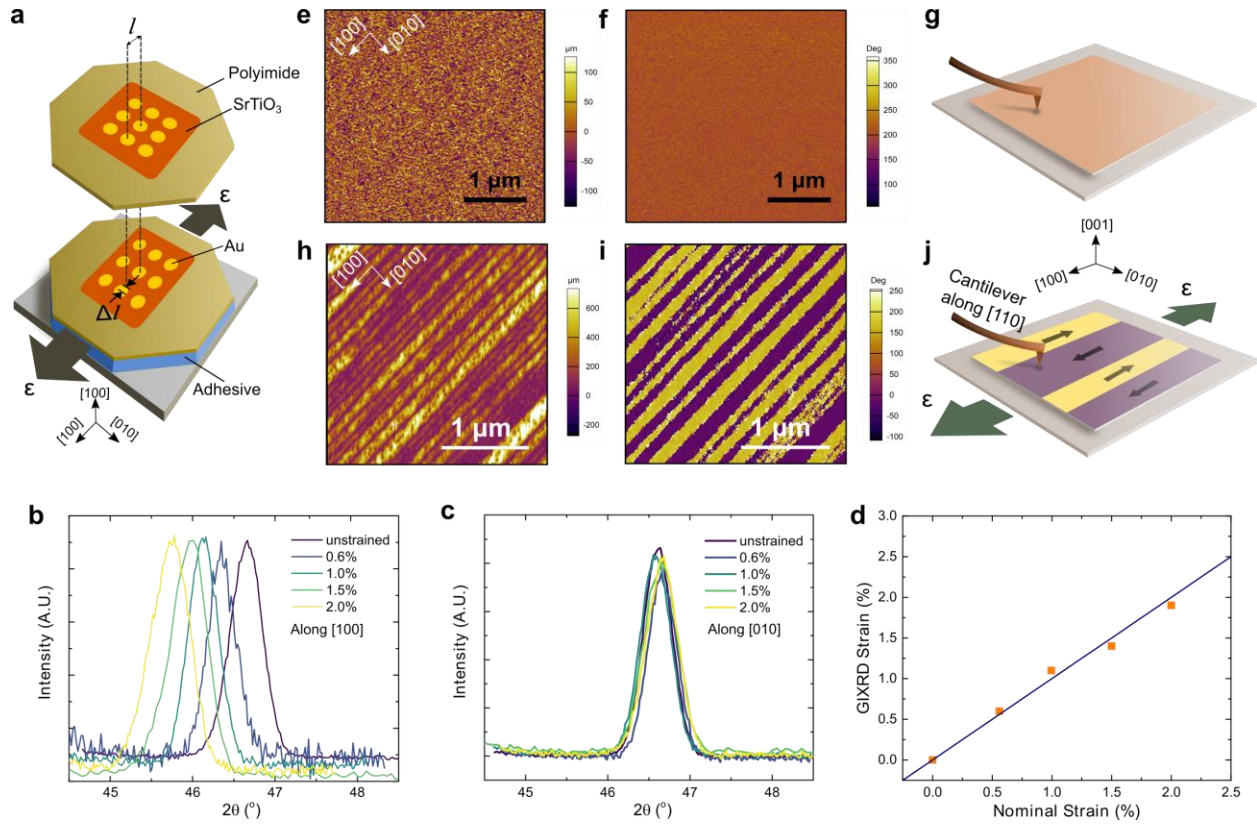


Figure 2 | Piezoresponse force microscopy (PFM) of room temperature ferroelectricity and grazing incidence X-ray diffraction (GIXRD) measurements in strained SrTiO₃ membranes.

a, Schematic illustrating the strain apparatus, wherein the SrTiO₃ membrane and polyimide sheet are stretched and fixed to a rigid substrate to maintain their strain state, with the ordered array of gold markers used for strain calibration. GIXRD results measured along **b**, [100] strain direction and **c**, [010] direction which was fixed to the unstrained state. **d**, Comparison of GIXRD strain and the optically measured nominal strain. The error bar is within the size of the marker. PFM amplitude **e** and phase **f** measured from unstrained membranes exhibit weak piezoresponse, indicating the absence of room-temperature ferroelectricity, illustrated in schematic **g**. PFM amplitude **h** and phase **i** measured from 2.0% uniaxially strained membranes exhibit room-temperature ferroelectricity with the notable 180° domain structure, illustrated in schematic **j**.

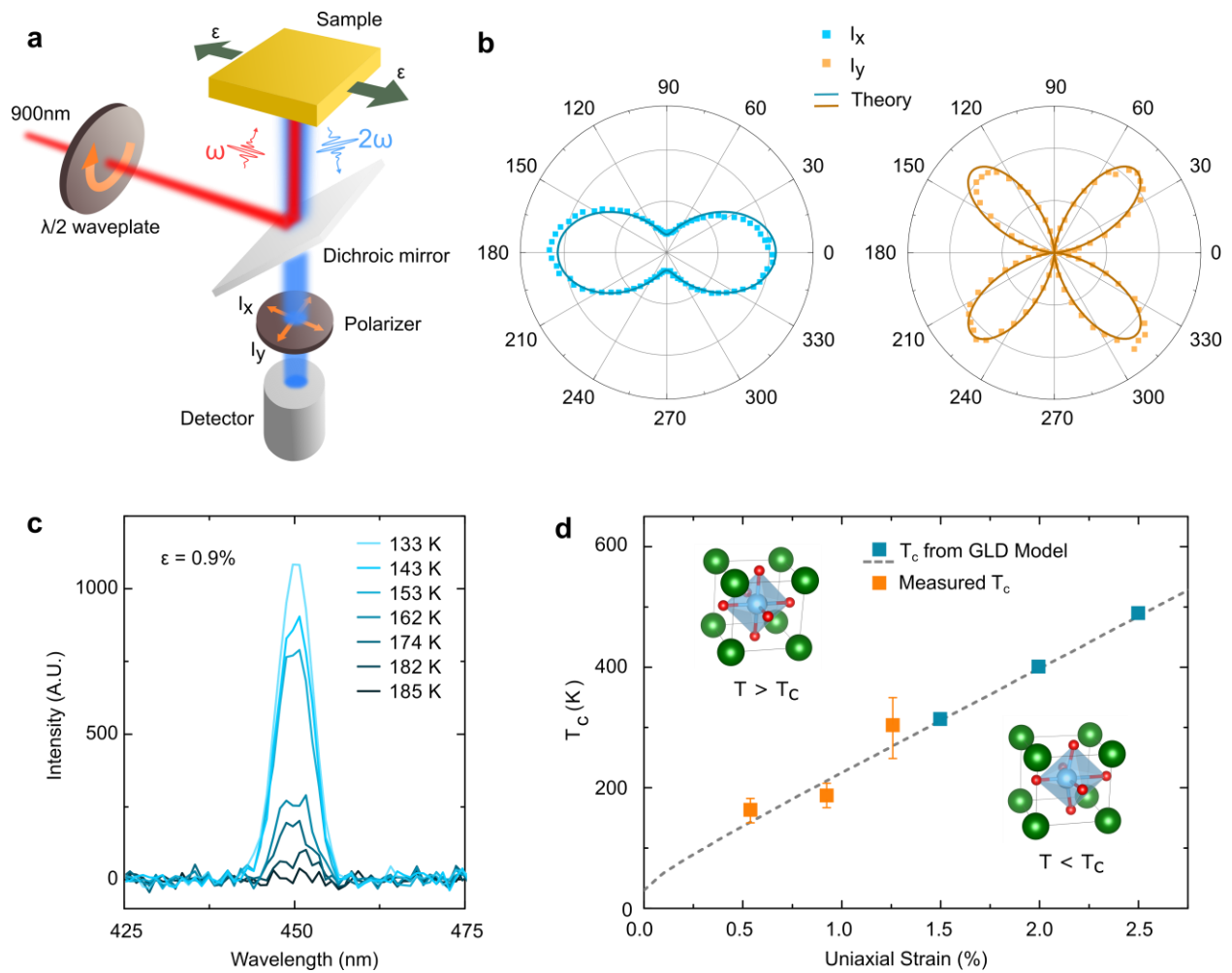


Figure 3 | Optical second harmonic generation (SHG) measurements of SrTiO_3 membranes.

a, Schematic illustrating the experimental setup for SHG measurements, wherein a 900 nm fundamental beam is used to excite the frequency-doubled signal from membranes in a reflection geometry that can be probed at a wavelength of 450 nm. **b**, SHG polar plots measured at room temperature as a function of incident beam polarization in membranes strained at 2.0%. **c**, SHG signals measured as a function of temperature in membranes strained at 0.9%. **d**, T_c plotted as a function of uniaxial strain directly measured from the SHG measurements, as well as high temperature extrapolations of the Ginsburg-Landau-Devonshire model.

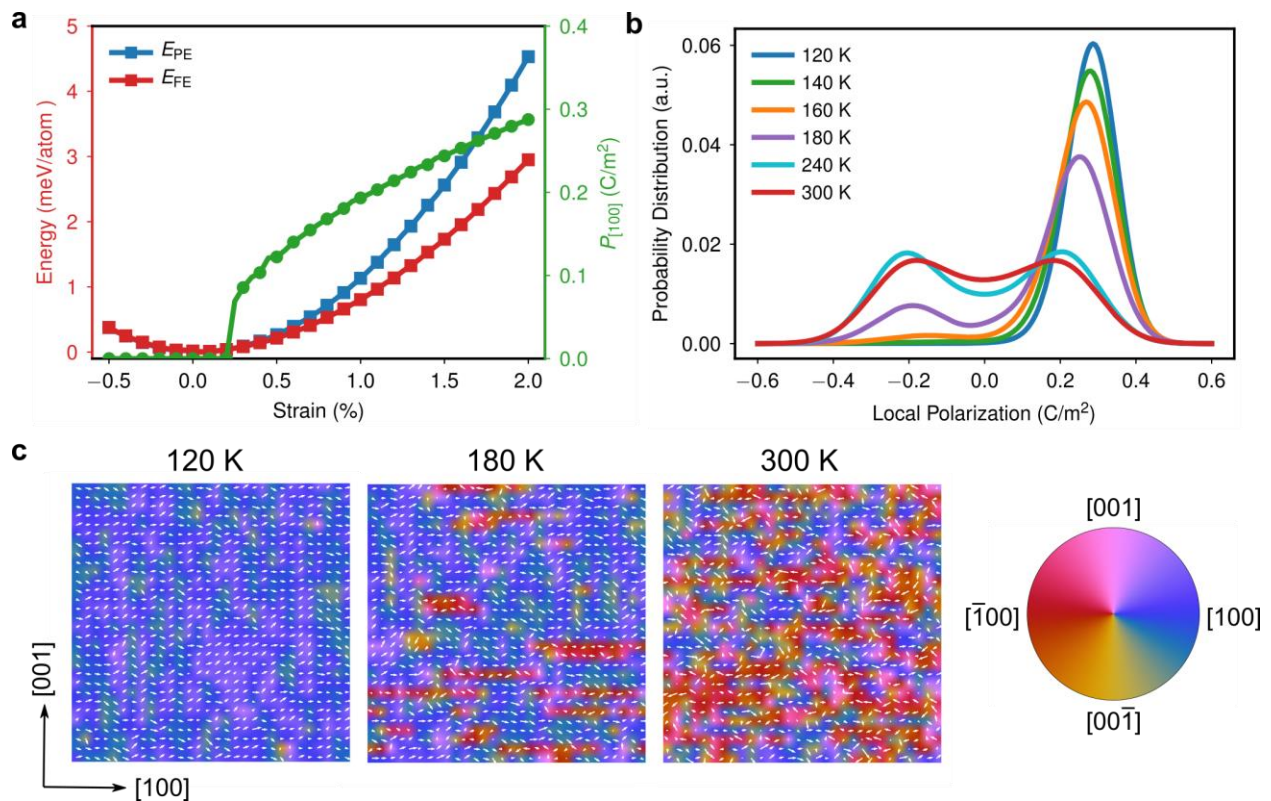


Figure 4 | First-principles density functional theory (DFT) calculations and molecular dynamics (MD) simulations. **a**, Calculated energy of paraelectric and ferroelectric phases and the induced ferroelectric polarization as a function of [100] uniaxial strain in SrTiO₃ from DFT calculations. **b**, Probability distributions of the unit cells adopting a [100]-component of local polarization at various temperatures. **c**, Snapshots of the dipole configurations at different temperatures obtained from MD simulations under 2.0% uniaxial strain conditions. Each white arrow in these graphs represents the local electric dipole within a unit cell, with a background color illustrating the polarization direction.

Acknowledgements

We acknowledge fruitful discussions with Ian R. Fisher during the course of this work. This work was supported by the U.S. Department of Energy, Office of Basic Energy Sciences (DOE-BES), Division of Materials Sciences and Engineering, under contract no. DE-AC02-76SF00515. S.C. and D.L. were supported by the Gordon and Betty Moore Foundation's Emergent Phenomena in Quantum Systems Initiative through grant no. GBMF4415. V.H. was supported by the Air Force Office of Scientific Research (AFOSR) Hybrid Materials MURI under award no. FA9550-18-1-0480. R.X. also acknowledges partial support from Stanford Geballe Laboratory for Advanced Materials (GLAM) Postdoctoral Fellowship program. S. L. acknowledges support from the Westlake Foundation. Work at the Molecular Foundry was supported by the Office of Science, Office of Basic Energy Sciences, of the U.S. Department of Energy under Contract No. DE-AC02-05CH11231.

Author contributions

R.X., H.Y.H., and D.L. conceived of the study. R.X., S.S.H., and S.C. designed the experiments. R.X. carried out the film synthesis, PFM characterization, and GLD calculations. J.H. and S.L. performed the DFT and MD simulations. R.X., E.S.B., E.K.W., and J.X. conducted the SHG measurements and analysis. R.X., T.J., V.H., and B.Y.W. performed the membrane fabrication. P.S., R.X., and S.S.H. carried out the GIXRD measurements. R.X., S.L., P.S., and H.Y.H. wrote the manuscript, with contributions from all authors.

Competing interests

The authors declare no competing interests.

References

1. Schooley, J. F., Hosler, W. R. & Cohen, M. L. Superconductivity in Semiconducting SrTiO₃. *Phys. Rev. Lett.* **12**, 474–475 (1964).
2. Zhong, W. & Vanderbilt, D. Competing structural instabilities in cubic perovskites. *Phys. Rev. Lett.* **74**, 2587–2590 (1995).
3. Ohtomo, A. & Hwang, H. Y. A high-mobility electron gas at the LaAlO₃/SrTiO₃ heterointerface. *Nature* **427**, 423–427 (2004).
4. Bi, F. *et al.* Room-temperature electronically-controlled ferromagnetism at the LaAlO₃/SrTiO₃ interface. *Nat. Commun.* **5**, 5019 (2014).
5. Li, L., Richter, C., Mannhart, J. & Ashoori, R. C. Coexistence of magnetic order and two-dimensional superconductivity at LaAlO₃/SrTiO₃ interfaces. *Nat. Phys.* **7**, 762–766 (2011).
6. Park, J. W. *et al.* Creation of a two-dimensional electron gas at an oxide interface on silicon. *Nat. Commun.* **1**, 94 (2010).
7. Zubko, P., Gariglio, S., Gabay, M., Ghosez, P. & Triscone, J.-M. Interface Physics in Complex Oxide Heterostructures. *Annu. Rev. Condens. Matter Phys.* **2**, 141–165 (2011).
8. Müller, K. A. & Burkard, H. SrTiO₃: An intrinsic quantum paraelectric below 4 K. *Phys. Rev. B* **19**, 3593–3602 (1979).
9. Pai, Y.-Y., Tylan-Tyler, A., Irvin, P. & Levy, J. Physics of SrTiO₃-based heterostructures and nanostructures: a review. *Reports Prog. Phys.* **81**, 036503 (2018).
10. Haeni, J. H. *et al.* Room-temperature ferroelectricity in strained SrTiO₃. *Nature* **430**, 758–761 (2004).
11. Li, Y. L. *et al.* Phase transitions and domain structures in strained pseudocubic (100) SrTiO₃ thin films. *Phys. Rev. B* **73**, 1–13 (2006).

12. Biegalski, M. D. *et al.* Influence of anisotropic strain on the dielectric and ferroelectric properties of SrTiO₃ thin films on DyScO₃ substrates. *Phys. Rev. B* **79**, 224117 (2009).
13. Warusawithana, M. P. *et al.* A ferroelectric oxide made directly on silicon. *Science* **34**, 367–371 (2009).
14. Vasudevarao, A. *et al.* Multiferroic domain dynamics in strained strontium titanate. *Phys. Rev. Lett.* **97**, 257602 (2006).
15. Mitsui, T. & Westphal, W. B. Dielectric and X-ray studies of Ca_xBa_{1-x}TiO₃ and Ca_xSr_{1-x}TiO₃. *Phys. Rev.* **124**, 1354–1359 (1961).
16. Itoh, M. *et al.* Ferroelectricity induced by oxygen isotope exchange in strontium titanate perovskite. *Phys. Rev. Lett.* **82**, 3540–3543 (1999).
17. Lee, D. *et al.* Emergence of room-temperature ferroelectricity at reduced dimensions. *Science* **349**, 1314–1317 (2015).
18. Schlom, D. G. *et al.* Strain tuning of ferroelectric thin films. *Annu. Rev. Mater. Res.* **37**, 589–626 (2007).
19. Choi, K. J., Biegalski, M., Li, Y. L., Sharan, A. & Schubert, J. Enhancement of ferroelectricity in strained BaTiO₃ thin films. *Science* **306**, 1005–1010 (2004).
20. Damodaran, A. R., Breckenfeld, E., Chen, Z., Lee, S. & Martin, L. W. Enhancement of ferroelectric curie temperature in BaTiO₃ films via strain-induced defect dipole alignment. *Adv. Mater.* **26**, 6341–6347 (2014).
21. Zeches, R. J. *et al.* A strain-driven morphotropic phase boundary in BiFeO₃. *Science* **326**, 977–981 (2009).
22. Martin, L. W., Chu, Y. H. & Ramesh, R. Advances in the growth and characterization of magnetic, ferroelectric, and multiferroic oxide thin films. *Mater. Sci. Eng. R Reports* **68**,

- 89–133 (2010).
23. Lu, D. *et al.* Synthesis of freestanding single-crystal perovskite films and heterostructures by etching of sacrificial water-soluble layers. *Nat. Mater.* **15**, 1255–1260 (2016).
 24. Hong, S. S. *et al.* Two-dimensional limit of crystalline order in perovskite membrane films. *Sci. Adv.* **3**, 5173 (2017).
 25. Ji, D. *et al.* Freestanding crystalline oxide perovskites down to the monolayer limit. *Nature* **570**, 87–90 (2019).
 26. Lu, D., Crossley, S., Xu, R., Hikita, Y. & Hwang, H. Y. Freestanding oxide ferroelectric tunnel junction memories transferred onto silicon. *Nano Lett.* **19**, 3999–4003 (2019).
 27. Singh, P. *et al.* Large-area crystalline BaSnO₃ membranes with high electron mobilities. *ACS Appl. Electron. Mater.* **1**, 1269–1274 (2019).
 28. Chen, Z. Y. *et al.* Freestanding crystalline YBa₂Cu₃O_{7-x} heterostructure membranes. *Phys. Rev. Mater.* **3**, 060801 (2019).
 29. Dong, G. *et al.* Super-elastic ferroelectric single-crystal membrane with continuous electric dipole rotation. *Science* **366**, 475–479 (2019).
 30. Hong, S. S. *et al.* Extreme tensile strain states in La_{0.7}Ca_{0.3}MnO₃ membranes. *Science* **368**, 71–76 (2020).
 31. Han, L. *et al.* Giant Uniaxial Strain Ferroelectric Domain Tuning in Freestanding PbTiO₃ Films. *Adv. Mater. Interfaces* 1901604 (2020).
 32. Kim, S. R. & Nairn, J. A. Fracture mechanics analysis of coating/substrate systems: Part II: Experiments in bending. *Eng. Fract. Mech.* **65**, 595–607 (2000).
 33. Denev, S. A., Lummen, T. T. A., Barnes, E., Kumar, A. & Gopalan, V. Probing ferroelectrics using optical second harmonic generation. *J. Am. Ceram. Soc.* **94**, 2699–2727

- (2011).
34. Qi, Y., Liu, S., Grinberg, I. & Rappe, A. M. Atomistic description for temperature-driven phase transitions in BaTiO₃. *Phys. Rev. B* **94**, 134308 (2016).
 35. Antons, A., Neaton, J. B., Rabe, K. M. & Vanderbilt, D. Tunability of the dielectric response of epitaxially strained SrTiO₃ from first principles. *Phys. Rev. B* **71**, 024102 (2005).
 36. Yadav, A. K. *et al.* Observation of polar vortices in oxide superlattices. *Nature* **530**, 198–201 (2016).
 37. Das, S. *et al.* Observation of room-temperature polar skyrmions. *Nature* **568**, 368–372 (2019).
 38. Pertsev, N. A., Tagantsev, A. K. & Setter, N. Phase transitions and strain-induced ferroelectricity in SrTiO₃ epitaxial thin films. *Phys. Rev. B* **61**, 825–829 (2000).
 39. Giannozzi, P. *et al.* QUANTUM ESPRESSO: A modular and open-source software project for quantum simulations of materials. *J. Phys. Condens. Matter* **21**, 395502 (2009).
 40. Ceperley, D. M. & Alder, B. J. Ground state of the electron gas by a stochastic method. *Phys. Rev. Lett.* **45**, 566–569 (1980).
 41. Garrity, K. F., Bennett, J. W., Rabe, K. M. & Vanderbilt, D. Pseudopotentials for high-throughput DFT calculations. *Comput. Mater. Sci.* **81**, 446–452 (2014).
 42. Pack, J. D. & Monkhorst, H. J. Special points for Brillouin-zone integrations. *Phys. Rev. B* **16**, 1748–1749 (1977).
 43. Marzari, N., Vanderbilt, D., De Vita, A. & Payne, M. C. Thermal contraction and disordering of the Al (110) surface. *Phys. Rev. Lett.* **82**, 3296–3299 (1999).
 44. Piskunov, S., Heifets, E., Eglitis, R. I. & Borstel, G. Bulk properties and electronic structure of SrTiO₃, BaTiO₃, PbTiO₃ perovskites: An ab initio HF/DFT study. *Comput. Mater. Sci.*

- 29**, 165–178 (2004).
45. Liu, S., Grinberg, I. & Rappe, A. M. Development of a bond-valence based interatomic potential for BiFeO₃ for accurate molecular dynamics simulations. *J. Phys. Condens. Matter* **25**, 102202 (2013).
 46. Wexler, R. B., Qi, Y. & Rappe, A. M. Sr-induced dipole scatter in Ba_xSr_{1-x}TiO₃: Insights from a transferable-bond valence-based interatomic potential. *Phys. Rev. B* **100**, 174109 (2019).
 47. Li, X. *et al.* Terahertz field-induced ferroelectricity in quantum paraelectric SrTiO₃. *Science* **364**, 1079–1082 (2019).
 48. Lu, H. *et al.* Asymmetry in mechanical polarization switching. *Appl. Phys. Lett.* **110**, 222903 (2017).
 49. Nosé, S. A unified formulation of the constant temperature molecular dynamics methods. *J. Chem. Phys.* **81**, 511–519 (1984).
 50. Plimpton, S. Fast parallel algorithms for short-range molecular dynamics. *J. Comput. Phys.* **117**, 1–19 (1995).

Supplementary Information

Strain-Induced Room-Temperature Ferroelectricity in SrTiO₃ Membranes

Ruijuan Xu^{*1,2}, Jiawei Huang³, Edward S. Barnard⁴, Seung Sae Hong^{1,2}, Prastuti Singh^{1,2},
Ed K. Wong⁴, Thies Jansen¹, Varun Harbola^{2,5}, Jun Xiao^{2,6}, Bai Yang Wang^{2,5}, Sam Crossley^{1,2},
Di Lu⁵, Shi Liu³, Harold Y. Hwang^{*1,2}

Email: rxu3@stanford.edu, hyhwang@stanford.edu

¹*Department of Applied Physics, Stanford University, Stanford, CA 94305, United States*

²*Stanford Institute for Materials and Energy Sciences, SLAC National Accelerator Laboratory,
Menlo Park, CA 94025, United States*

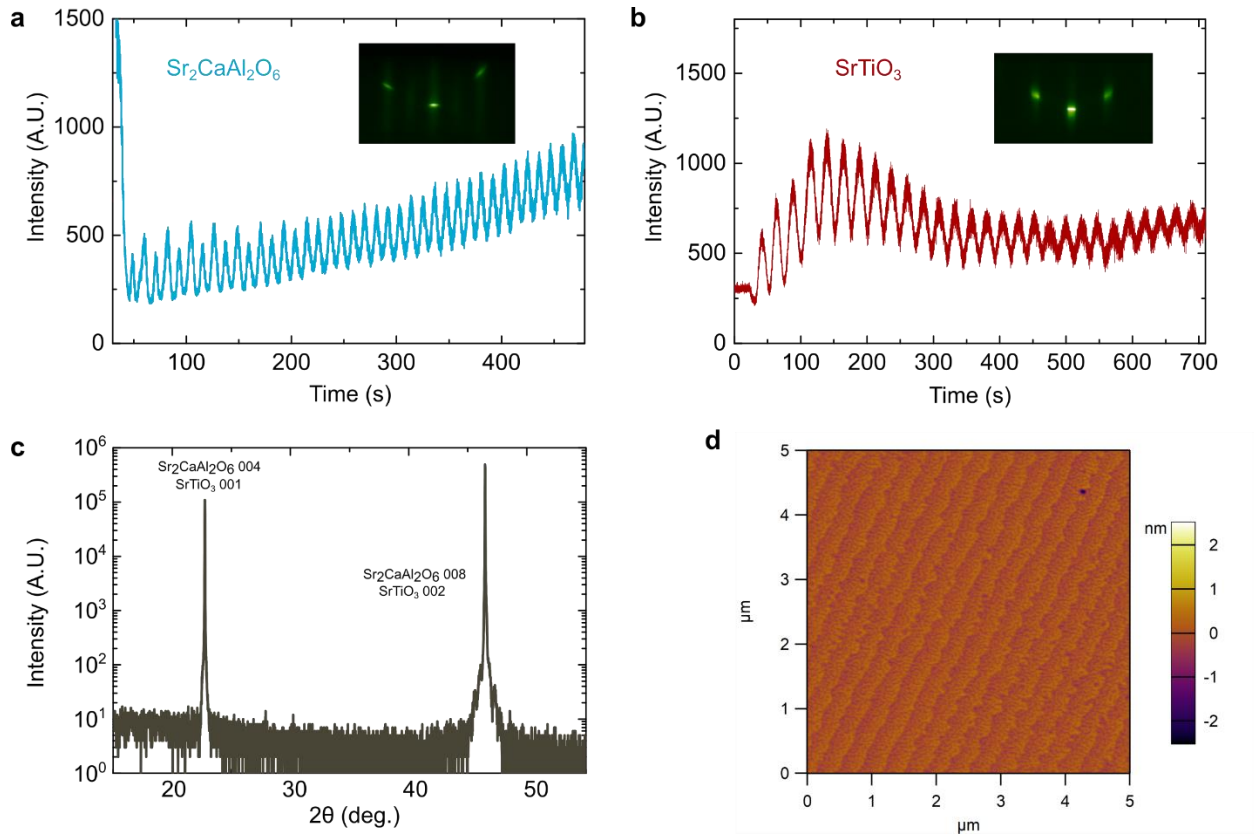
³*School of Science, Westlake University, Hangzhou, Zhejiang 310012, China*

⁴*The Molecular Foundry, Lawrence Berkeley National Laboratory, 1 Cyclotron Road, Berkeley,
CA 94720, United States*

⁵*Department of Physics, Stanford University, Stanford, CA 94305, United States*

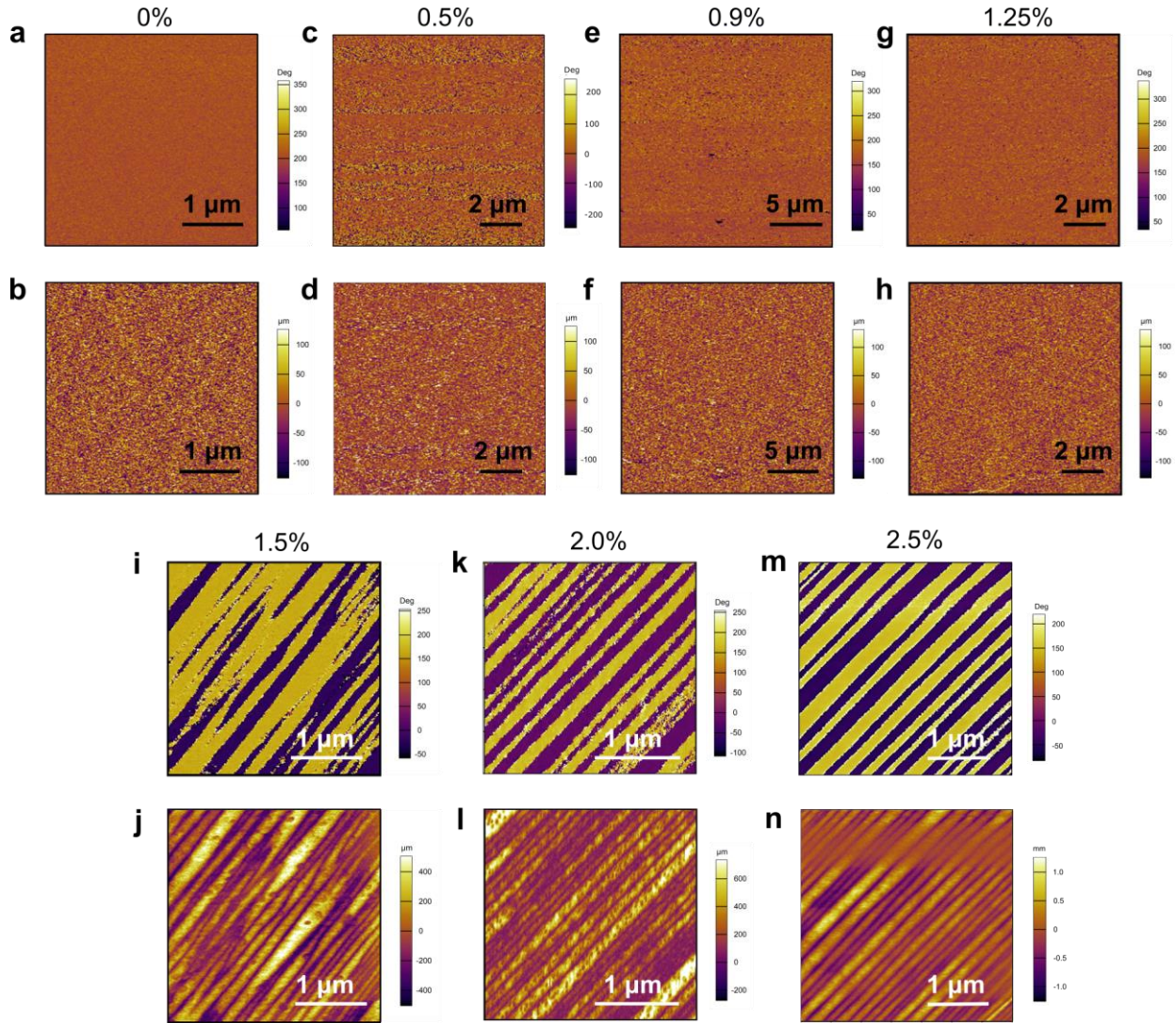
⁶*Department of Materials Science and Engineering, Stanford University, Stanford, CA 94305,
United States*

Supplementary Figure 1



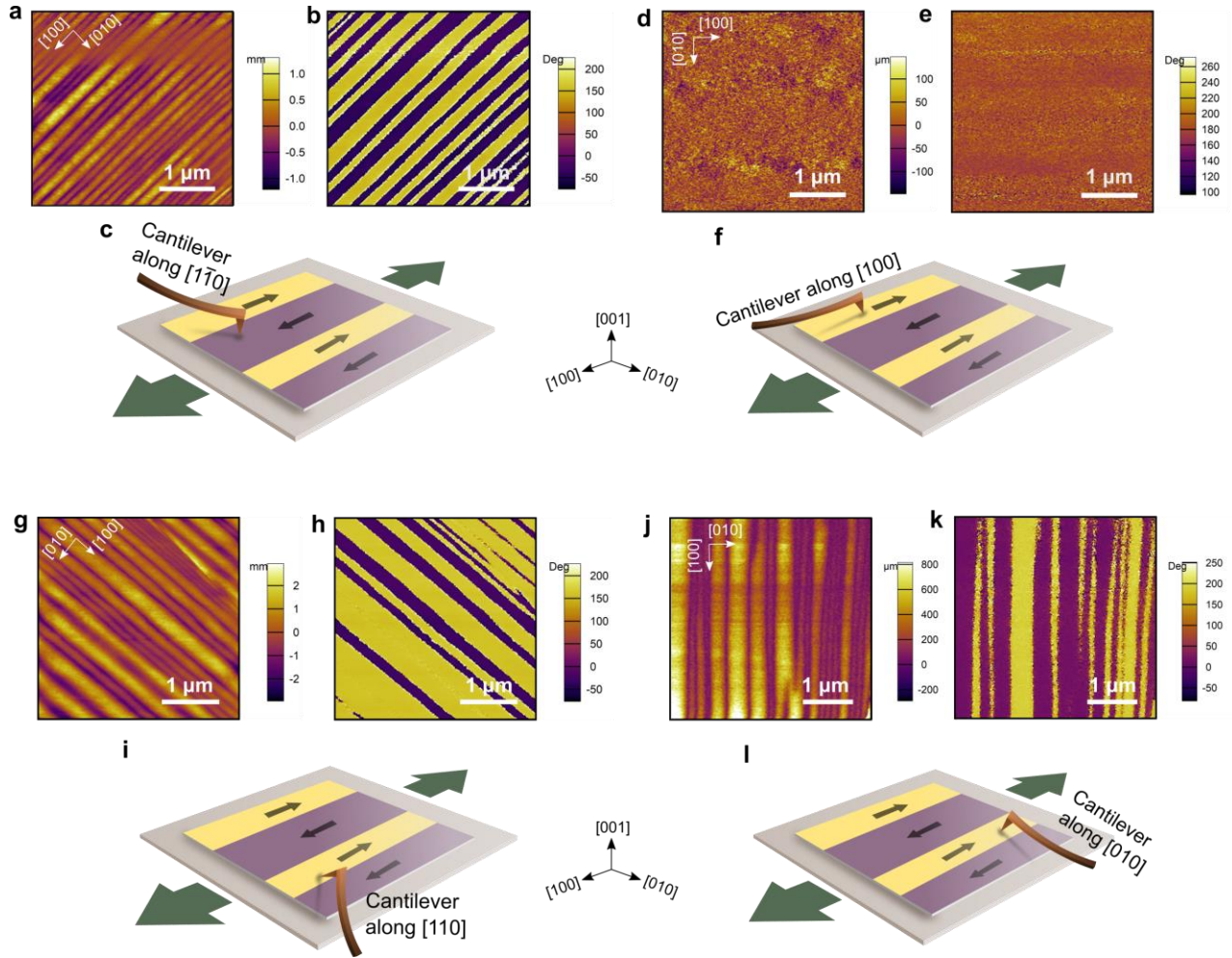
Supplementary Figure 1 | Growth and structural characterization of SrTiO₃/Sr₂CaAl₂O₆/SrTiO₃ heterostructure. Reflection high-energy electron diffraction (RHEED) oscillations and patterns of **a**, Sr₂CaAl₂O₆ and **b**, SrTiO₃, which indicate typical layer-by-layer 2D growth mode. **c**, $\theta - 2\theta$ X-ray diffraction scans showing a single diffraction peak with all layer peaks overlapping together due to the small lattice mismatch between the different film layers. **d**, Atomic force microscopy characterization of as-grown SrTiO₃ films showing an atomically smooth surface with unit cell step terraces.

Supplementary Figure 2



Supplementary Figure 2 | Room-temperature piezoresponse force microscopy (PFM) characterization of strained SrTiO₃ membranes. Lateral PFM phase and amplitude of membranes uniaxially strained at **a, b**, 0%; **c, d**, 0.5%; **e, f**, 0.9%; **g, h**, 1.25%; **i, j**, 1.5%; **k, l**, 2.0%; **m, n**, 2.5%, respectively, wherein room-temperature ferroelectricity is observed to emerge at 1.5% strain, which is characterized by the 180° ferroelectric polydomain patterns.

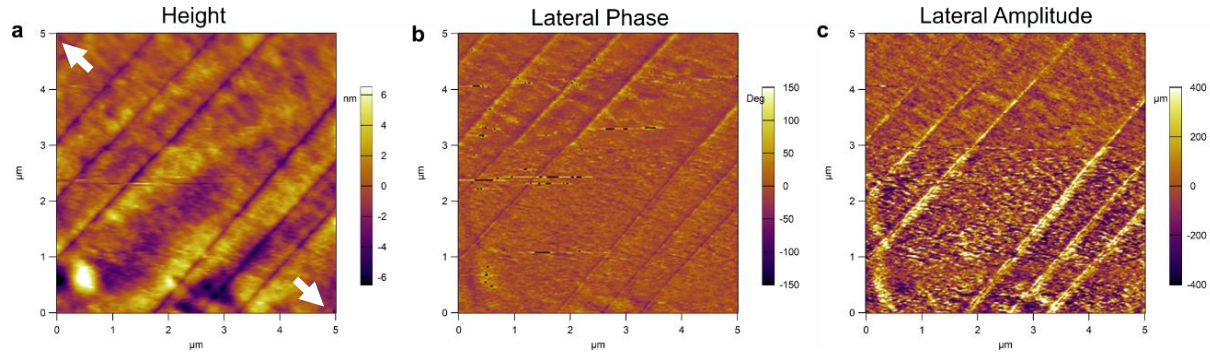
Supplementary Figure 3



Supplementary Figure 3 | Piezoresponse force microscopy (PFM) characterization of domain structures in 2.5% strained SrTiO₃ membranes. Lateral PFM amplitude and phase measured by aligning the PFM cantilever along the **a, b**, $[1\bar{1}0]$, **d, e**, $[100]$, **g, h**, $[110]$, and **j, k**, $[010]$ directions, respectively. Whereas evident ferroelectric stripe domain patterns are observed when scanning along the $[1\bar{1}0]$, $[110]$, and $[010]$ directions, the piezoresponse vanishes when scanning along $[100]$, indicating the in-plane polarization of the ferroelectric domains is aligned along $[100]/[1\bar{1}0]$, with the adjacent domains polarized at a 180° difference. The measurement process is illustrated in **c, f, i**, and **l**. These results clearly show that the polarization of these domain features

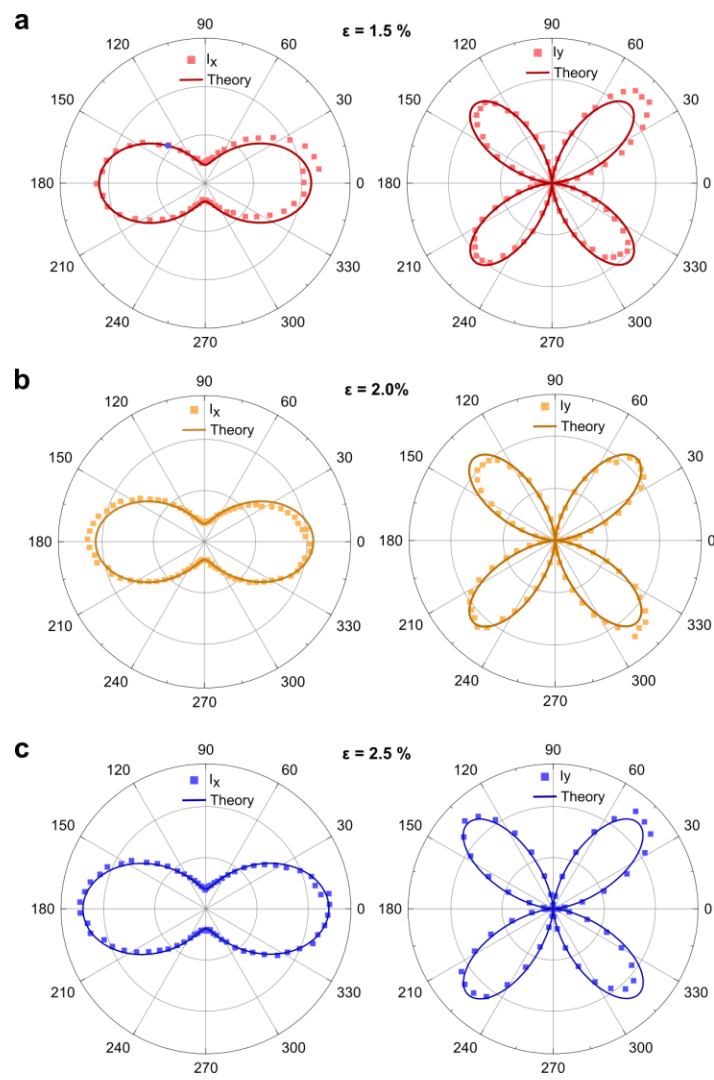
align along specific crystallographic directions, which evidences the presence of ferroelectricity, whereas other mechanisms of induced ferroelectric-like PFM response are typically invariant with respect to the cantilever scan orientation.

Supplementary Figure 4



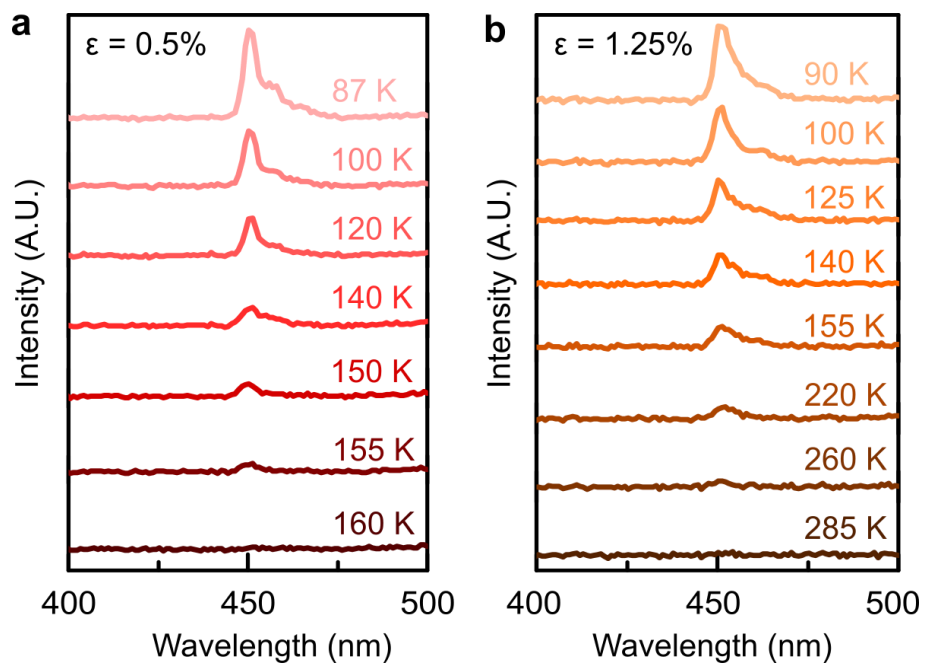
Supplementary Figure 4 | Piezoresponse Force Microscopy (PFM) characterization of strained SrTiO₃ membranes beyond the threshold for crack formation. a, PFM height image shows cracks perpendicular to the uniaxial strain direction. White arrows here illustrate the uniaxial strain direction along [100]. **b**, Lateral phase and **c**, amplitude images show the absence of 180° degree domains in cracked SrTiO₃ membranes.

Supplementary Figure 5



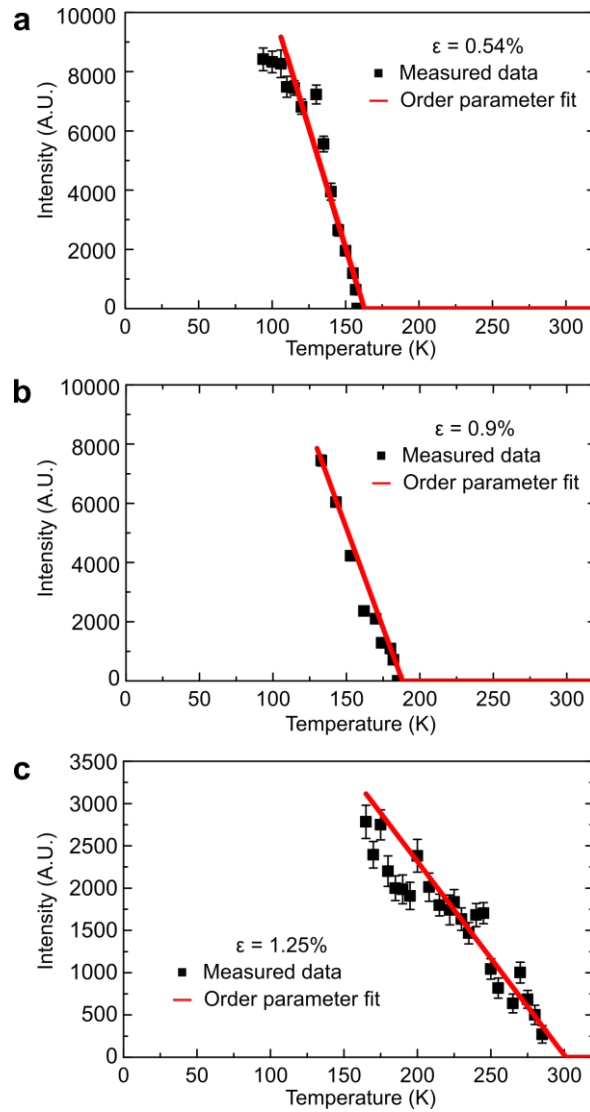
Supplementary Figure 5 | Optical second harmonic generation (SHG) measurements of SrTiO₃ membranes. SHG polar plots measured at room temperature as a function of incident beam polarization in membranes strained at **a**, 1.5%, **b**, 2.0%, **c**, 2.5%.

Supplementary Figure 6



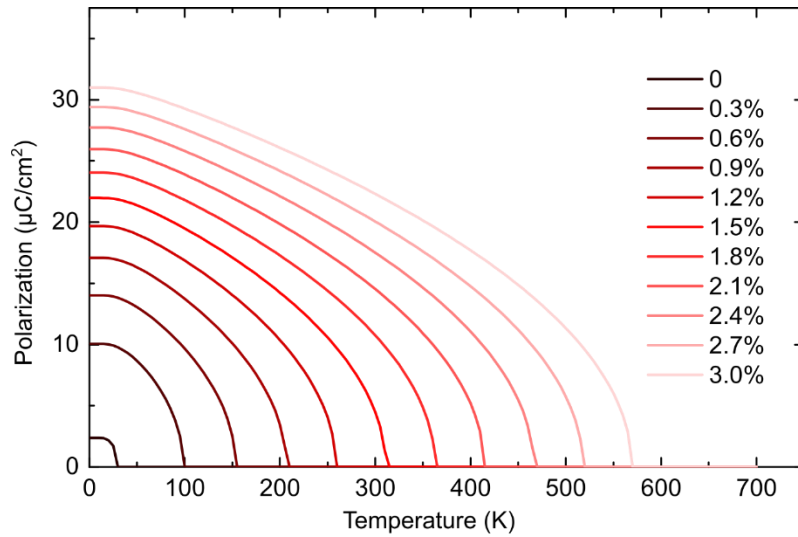
Supplementary Figure 6 | Temperature-dependent second harmonic generation (SHG) measurements of strained SrTiO₃ membranes. SHG measurements performed on SrTiO₃ membranes as a function of temperature. The membranes are uniaxially strained at **a**, 0.5% and **b**, 1.25%.

Supplementary Figure 7



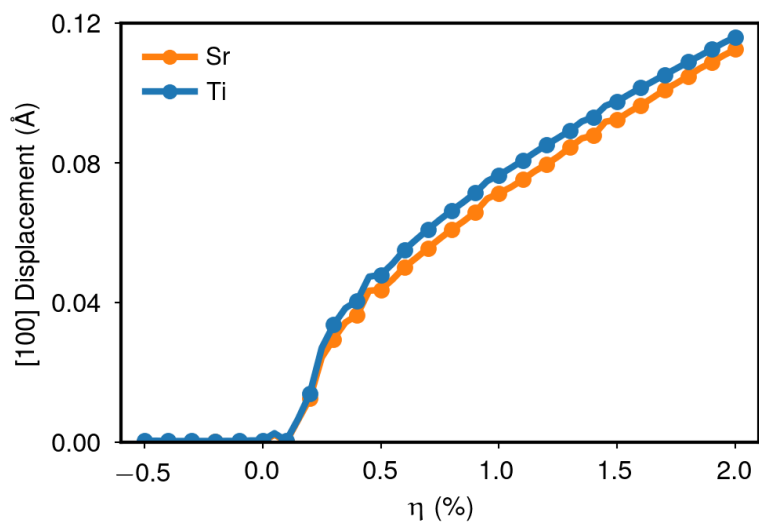
Supplementary Figure 7 | Extracting T_c from SHG results for each strain state. Here, since the SHG intensity $\propto P_1^2$ while $P_1 \propto T^{1/2}$ (within the Ginsburg-Landau-Devonshire model), we can derive that the SHG intensity $\propto T$. Plotting the integrated SHG peak intensity as a function of temperature for membranes uniaxially strained at **a**, 0.54%, **b**, 0.9%, and **c**, 1.25%, the T_c can be extracted for each strain state with this linear intensity-temperature relationship.

Supplementary Figure 8



Supplementary Figure 8 | The calculated polarization evolution with temperature at different uniaxial strain states. Temperature-dependent polarization evolution as a function of applied uniaxial strain along [100] is calculated using the Ginsburg-Landau-Devonshire model. The relation between the transition temperature T_c and strain can be further extracted at $P = 0$.

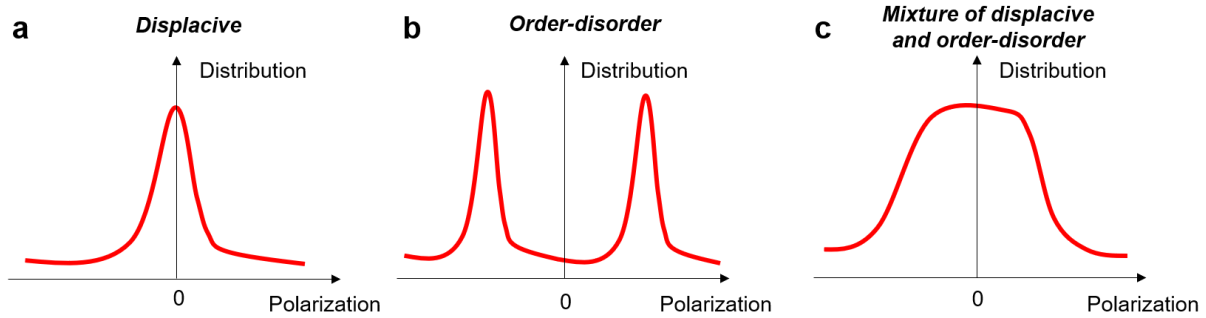
Supplementary Figure 9



Supplementary Figure 9 | The local displacements of Sr and Ti atoms calculated by DFT.

Both the Sr and Ti atoms in SrTiO₃ displace along the [100] direction in response to the uniaxial strain along [100].

Supplementary Figure 10



Supplementary Figure 10 | Schematics of the characteristic polarization distribution near

the phase transition. The polarization distribution in the paraelectric phase for **a**, displacive, **b**, order-disorder, and **c**, a mixture of the two. In the ferroelectric phase of strained SrTiO₃, the displacive character dominates at lower temperature, as the distribution of local polarization has a single peak and the peak position shifts toward lower polarization values with increasing temperature. When the temperature rises close to T_c , the order-disorder character dominates, shown as a double-peak in the distribution curve. However, an ideal order-disorder character will have the two peaks well separated in the high temperature phase (Fig. 4b). Therefore, even at a temperature close to T_c , the displacive character still plays a role, indicating a mixture of displacive and order-disorder transition characteristics in SrTiO₃.

Supplementary Table 1. DFT calculated structural evolution with uniaxial strain

<i>Strain</i>	<i>a</i> (Å)	<i>b</i> (Å)	<i>c</i> (Å)	<i>P_x</i> (C/m ²)	<i>P_y</i> (C/m ²)	<i>P_z</i> (C/m ²)
-0.5	3.8377	3.857	3.8617	0.001	0	0
-0.45	3.8396	3.857	3.8617	0.001	0	0
-0.4	3.8416	3.857	3.8606	0.001	0	0
-0.35	3.8435	3.857	3.86	0.001	0	0
-0.3	3.8454	3.857	3.8595	0.001	0	0
-0.25	3.8474	3.857	3.859	0.001	0	0
-0.2	3.8493	3.857	3.8586	0.001	0	0
-0.15	3.8512	3.857	3.8578	0.001	0	0
-0.1	3.8531	3.857	3.8573	0.001	0	0
-0.05	3.8551	3.857	3.8548	0.001	0	0
0	3.857	3.857	3.8548	0.001	0	0
0.05	3.8589	3.857	3.8554	-0.007	0	0
0.1	3.8609	3.857	3.855	0.001	0	0
0.15	3.8628	3.857	3.8543	0.018	0	0
0.2	3.8647	3.857	3.8539	0.037	0	0
0.25	3.8666	3.857	3.8534	0.072	0.001	0
0.3	3.8686	3.857	3.8529	0.09	0.001	0
0.35	3.8705	3.857	3.8525	0.103	0.001	0
0.4	3.8724	3.857	3.8516	0.109	0.001	0
0.45	3.8744	3.857	3.8515	0.128	0.001	0
0.5	3.8763	3.857	3.8508	0.129	0.001	0
0.55	3.8782	3.857	3.8501	0.137	0.002	0
0.6	3.8801	3.857	3.8496	0.148	0.002	0
0.65	3.8821	3.857	3.8493	0.156	0.002	0
0.7	3.884	3.857	3.8488	0.164	0.002	0
0.75	3.8859	3.857	3.8482	0.171	0.002	0
0.8	3.8878	3.857	3.8472	0.178	0.002	0
0.85	3.8898	3.857	3.8466	0.185	0.002	0
0.9	3.8917	3.857	3.8466	0.192	0.003	0
0.95	3.8936	3.857	3.8455	0.202	0.003	0
1	3.8956	3.857	3.8454	0.206	0.003	0
1.05	3.8975	3.857	3.8448	0.211	-0.007	0.001
1.1	3.8994	3.857	3.8443	0.217	-0.007	0.001
1.15	3.9013	3.857	3.8417	0.224	-0.007	0.001
1.2	3.9033	3.857	3.8425	0.229	-0.007	0.001
1.25	3.9052	3.857	3.8405	0.235	-0.007	0.001
1.3	3.9071	3.857	3.8412	0.241	-0.007	0.001
1.35	3.9091	3.857	3.8405	0.248	-0.008	0.001
1.4	3.911	3.857	3.8385	0.251	-0.006	0.001
1.45	3.9129	3.857	3.84	0.26	-0.011	0.002

<i>1.5</i>	3.9148	3.857	3.8395	0.263	-0.013	0.003
<i>1.55</i>	3.9168	3.857	3.8383	0.269	-0.011	0.003
<i>1.6</i>	3.9187	3.857	3.8384	0.274	-0.012	0.004
<i>1.65</i>	3.9206	3.857	3.8376	0.279	-0.012	0.004
<i>1.7</i>	3.9226	3.857	3.8371	0.284	-0.014	0.001
<i>1.75</i>	3.9245	3.857	3.8366	0.289	-0.014	0.002
<i>1.8</i>	3.9264	3.857	3.8354	0.294	-0.013	0.002
<i>1.85</i>	3.9284	3.857	3.8356	0.299	-0.016	-0.001
<i>1.9</i>	3.9303	3.857	3.8349	0.304	-0.013	0.003
<i>1.95</i>	3.9322	3.857	3.8342	0.309	-0.012	0.003
<i>2</i>	3.9341	3.857	3.8336	0.314	-0.009	0.003

Supplementary Table 2. Landau Free Energy Parameters for SrTiO₃

<i>Parameters</i>	<i>Value (in cgs units, temperature in K)</i>
α_1	$4.5[\coth\left(\frac{54}{T}\right) - \coth\left(\frac{54}{30}\right)] \times 10^{-3}$
α_{11}	2.5×10^{-12}
α_{12}	1.5×10^{-12}
c_{11}	3.36×10^{12}
c_{12}	1.07×10^{12}
c_{44}	1.27×10^{12}
g_{11}	1.39
g_{12}	-0.12
g_{44}	0.27
β_{11}	1.94×10^{43}
β_{12}	3.96×10^{43}
λ_{11}	1.3×10^{27}
λ_{12}	-2.5×10^{27}
λ_{44}	-2.3×10^{27}
t_{11}	-3.74×10^{15}
t_{12}	0.15×10^{15}
t_{44}	7.0×10^{15}